Building Color-Management Modules Using Linear Optimization I. Desktop Color System

Koichi Iino* and Roy S. Berns†

Munsell Color Science Laboratory, Chester F. Carlson Center for Imaging Science, Rochester Institute of Technology, 54 Lomb Memorial Drive, Rochester, New York, 14623-5604

**Manufacturing Research Lab., Technical Research Institute, Toppan Printing Co., Ltd., 4-2-3 Takanodai-Minami, Sugito-Machi, Kitakatsusika-Gun, Saitama 345-8508, Japan*

Two kinds of models were derived that predicted spectral reflectance factor of colors formed using an ink-jet printer. One was the spectral Murray–Davies–Yule–Nielsen model in which n-value was assumed to vary as a function of wavelength. The other was based on the Omatsu model in which the path length of light scattering was assumed to vary as a function of wavelength. Model parameters were optimized using a test target of 57 samples consisting of cyan, magenta, yellow, red, green, blue, and black colors varying between white and the maximum ink amount. Average accuracy of an independent data set sampling the printer's color gamut was 4.2 and 3.9 ΔE^*_{ab}, for the Murray–Davies–Yule–Nielsen and the Omatsu models, respectively. The difference in performance was not significant. The Yule–Nielsen model was selected to build device profiles because of its simplicity in comparison to the Omatsu model. A desktop scanner was colorimetrically characterized using a multiple-linear-regression model to build a concatenated device profile in which digital counts of a scanned photographic reflection print were the input and those of the printer were the output. Because the printer model was analytically noninvertable, the Newton–Raphson and the Simplex iterative methods were evaluated as candidate optimization methods to build $33 \times 33 \times 33$ color look-up tables. These tables were evaluated by comparing a photographic reflection IT8.7/2 target with its printed reproduction. The Simplex method yielded superior results, particularly for colors near the edge or outside of the printer's color gamut. The average ΔE^*_{ab} error from a profile based on the Simplex method was 5.9 including colors outside of the printer's color gamut.

Journal of Imaging Science and Technology 42: 79–94 (1998)

Introduction

Device-independent color[1] is now recognized as a general way of color communication for electronic devices. Although terminology varies, obtaining acceptable color reproductions requires: colorimetric device characterization, color appearance modeling, and color gamut mapping. A colorimetric device characterization is a set of equations or a three-dimensional data set that converts between the device's signal space and a colorimetric space such as tristimulus or CIELAB space. Appearance models account for differences in illuminating, viewing, and cognitive conditions between different imaging modalities. Gamut mapping often consists of a set of rules to map the gamut volume defined using a color-appearance space of one device onto a second device. Once the input and output imaging devices are identified, the three stages are used to build a color-management module or CMM. This is usually in the form of a three-dimensional color look-up table (CLUT). Linear interpolation is used to estimate values in between CLUT entries.

When considering the colorimetric characterization of desktop color devices, three methods are commonly used: direct interpolation, multiple-linear regression, and analytical modeling. For the first two methods, one first generates a test target sampling the device's input space (for RGB devices, d_r, d_g, and d_b and for CMYK devices, d_c, d_m, d_y, and d_k, where d represents digital counts) that is measured colorimetrically for a defined observer and illuminant. This can vary between hundreds and thousands of samples.[2,3] In a sense, the first two methods are the extrema of a single empirical approach. Direct interpolation[2–5] can be thought of as a piecewise linear model while multiple-linear regression[6,7] represents a single linear or nonlinear model. If the relationship between digital and colorimetric representations is highly nonlinear, direct interpolation yields higher accuracy (though constrained by the sampling). As the relationship becomes more linear, the two methods yield equivalent results. It is also possible, and desirable, to blend the two methods.

The third method is to derive an analytical model that relates input drive signals to spectral output. When scanning, digital data are used to predict the spectral reflectance factor or spectral transmittance of the scanned photographic material.[8–12] In similar fashion, printing models relate drive signals to spectral reflectance factor.[13–19] For CRT displays, the input drive signals are related to spectral radiance or irradiance.[20,21] Spectral data are used to calculate colorimetry for a defined illuminant (in the case of scanning and printing) and observer. Test targets are produced that enable the determination of the model's parameters. Because most theoretical models have practical limitations, the parameters are statistically estimated. Thus, strictly speaking, analytical models are a combination of theory and empiricism. However, because the empirically determined parameters can be theoretically related to the device's physics, it seems reasonable to consider this approach as an analytical method.

Original manuscript received April 2, 1997

† IS&T Member

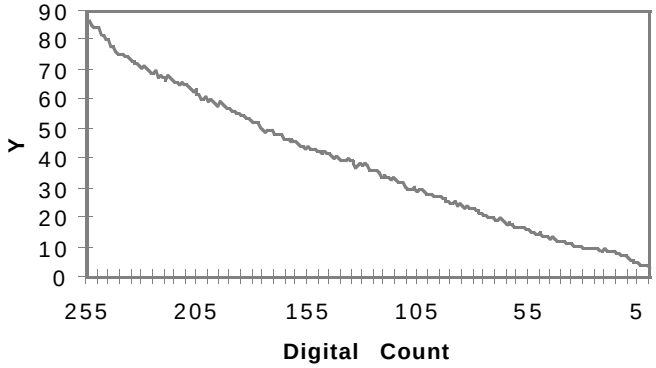

Figure 1. Relationship between digital counts and reproduced luminance factors of black ink.

There are several advantages to using analytical models. First, a small number of samples is required to build the model. As a consequence, one can update a device profile readily with changes in consumables. Second, they provide excellent modeling tools for making engineering improvements in a device (e.g., estimating the effects of changing an ink's spectral characteristics or halftoning algorithm on image quality) or in device calibration (e.g., set up of a display to achieve optimal tone reproduction[20,21]). Third, one can calculate colorimetric values for any illuminant and observer of choice that enables easy integration with color appearance models. Finally, they minimize problems from linear subsampling in highly nonlinear subspaces and extrapolation when building device profiles and CMMs.

One limitation when using analytical models to build printer device profiles is that they are usually noninvertable. Analytical models are derived from device drive signals. To build a printer profile, one inputs colorimetric coordinates and calculates device coordinates numerically. The particular numerical method affects the accuracy of the CLUT.

Thus, we were interested in exploring several issues relating to building a CMM for a desktop color system consisting of a flat-bed scanner and ink-jet printer. The first issue was evaluating the accuracy of two different analytical models: Murray–Davies–Yule–Nielsen and Omatsu. The second issue was evaluating the efficacy of two numerical methods: Newton–Raphson and Simplex.

Experimental

Output Device. An Apple StyleWriter Pro printer was used in this research. This is a four-color (cyan, magenta, yellow, and black), thermal ink-jet printer that employs a halftone process to achieve tone modulation. It is considered an RGB printer. Through its software, d_r, d_g, and d_b, data are converted to area modulation of cyan, magenta, yellow, and black ink. The "Best" print quality option was selected yielding the highest spatial image quality and largest color gamut using Apple Premium Coated paper.

Two halftoning algorithms are available: Scatter and Pattern. The Scatter mode utilizes FM stochastic screening that blends colors in a random scattering of dots. The Pattern mode provides a repeating pattern of dots. In Pattern mode, dots of two primaries except black ink are placed in the same location, frequently referred to as dot-on-dot,[22] concentric dot, or cluster dot. The dots of black ink, in theory, never overlap the other colors. For perfect dot placement, this image microstructure yields printable colors composed of a primary (cyan, magenta, or yellow), a secondary (red, green, or blue), black, and paper. The Pattern mode was selected as the halftoning process for this research based on the assumption that the RGB to CMYK conversion was equivalent to a 100% gray-component replacement algorithm. For some printers, the Scatter mode, recommended for pictorial images, has a more complicated conversion. If the conversion is not known, an analytical model cannot be derived. Thus for the Pattern mode, the conversion from d_r, d_g, and d_b digital counts in the RGB space to the drive signals d_c, d_m, d_y, and d_k, of each primary ink for an 8-bit digital representation is described using the 100% gray-component replacement algorithm as follows:

$$\begin{aligned} d_k &= \min(255 - d_r,\ 255 - d_g,\ 255 - d_b), \\ d_c &= 255 - d_r - d_k, \\ d_m &= 255 - d_g - d_k, \\ d_y &= 255 - d_b - d_k. \end{aligned} \tag{1}$$

To investigate the size of the halftone cell, 256 color patches of a single primary color were printed and measured colorimetrically. The relationship between digital counts and luminance factor of the black ink is shown in Fig. 1. From visual observations under magnification, this printer obviously does not have 256 quantization levels. However, it was difficult colorimetrically to find breakthrough levels indicating halftone cell size due to the extremely small differences in luminance factor between each sample. Noise in the measurements obscured the quantization. In addition, it appears that the breakthrough levels are spaced nonlinearly. Therefore, it was assumed that the spectral reflectance factor would vary smoothly with a change of digital data. Accordingly, modeling and verification targets were designed.

A modeling target was printed consisting of ramps of each single color type: cyan (C), magenta (M), yellow (Ye), and black (K); and each two-color overprint: red (R), green (G), and blue (B). Each ramp had 9 steps with a range from 0 to 255 digital counts in intervals of 32 digital count in the RGB space. The total number of samples including the paper equaled 57.

A verification target, used to estimate forward model performance, was also printed. The target was 125 colors based on a digital $5 \times 5 \times 5$ factorial design sampling the RGB space. These samples were not contained within the modeling target except the paper white.

Input Device. A Sharp JX-610 color-image scanner was selected as an input device. This is a single-pass three-fluorescent-source flatbed CCD scanner capable of 600 dpi spatial resolution. The scanner settings were adjusted so that an Eastman Kodak Ektacolor Q-60R1 IT8.7/2 (Ref. 23) reflection target had its black and white image areas nearly 0 and 255 digital counts for each channel and its tone reproduction reasonable when displayed on a CRT monitor viewed in dim ambient lighting conditions. The photographic target was used to develop a colorimetric characterization for this scanner and Ektacolor paper.

Metrology. The spectral reflectance factors of both the printed samples and the IT8.7/2 photographic target were measured using a Gretag SPM 60 spectrophotometer. This instrument has 45°/0° geometry and samples the spectrum from 380 to 730 nm in 10-nm increments and bandpass. Each sample was measured in contact with a black mat surface. Colorimetric data were calculated for illuminat D_{65} and the 1931 2° standard observer using ASTM tristimulus weights.[24]

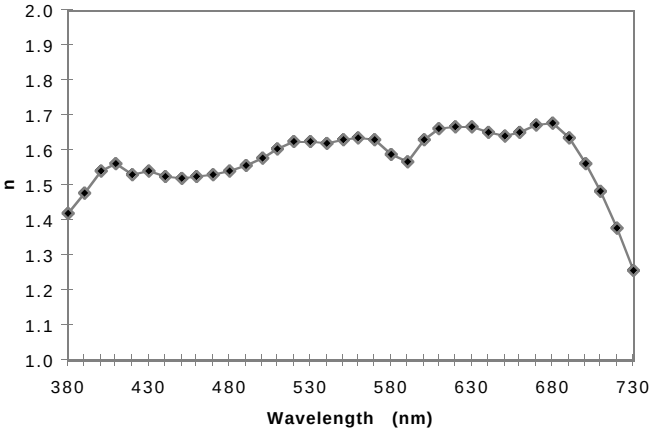

Figure 2. Yule–Nielsen's n-values as a function of wavelength.

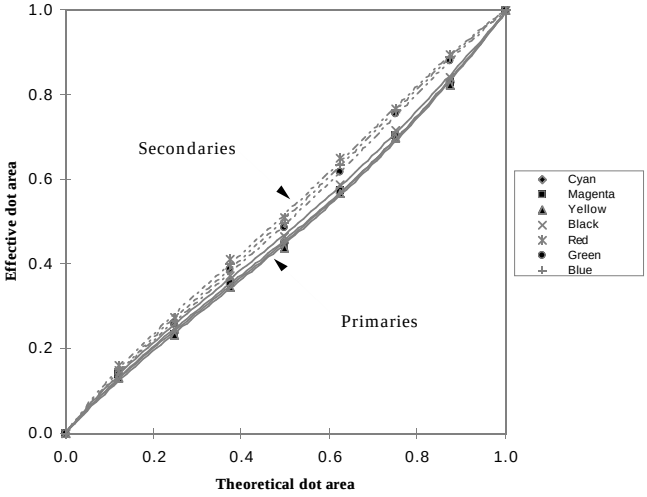

Figure 3. Relationship between theoretical dot area and statistically derived effective dot area. Lines joining data were derived using forth-order polynomial models.

Printer Forward Models

As described, the dot-on-dot halftone pattern yields, at most, four simultaneous colors (including paper). Thus, the relationship between the drive signals shown in Eq. 1 and the theoretical dot areas of each color type (a_c, a_m, a_y, a_k, a_r, a_g, a_b, and a_w) is expressed by Eq. 2.

$$\begin{aligned}
a_r &= \min(d_m, d_y)/255,\\
a_g &= \min(d_c, d_y)/255,\\
a_b &= \min(d_c, d_m)/255,\\
a_c &= d_c/255 - a_g - a_b,\\
a_m &= d_m/255 - a_r - a_b,\\
a_y &= d_y/255 - a_r - a_g,\\
a_k &= d_k/255,\\
a_w &= 1 - a_r - a_g - a_b - a_c - a_m - a_y - a_k.
\end{aligned} \tag{2}$$

Spectral Murray–Davies Model Modified by Yule–Nielsen *n* Correction. The Murray–Davies equation,[25] which predicts the reflectance factor R in a monochrome halftone process using dot area a_{ink} and reflectance factors of both solid ink R_{ink} and paper R_w, is extended to the spectral level.

$$R_\lambda = a_{\text{ink}} R_{\lambda,\text{ink}} + (1 - a_{\text{ink}}) R_{\lambda,w}. \tag{3}$$

In its usual wideband implementation, the measured reflectance factor is darker than that predicted by the Murray–Davies equation. This error is caused by the effect of light scattering within the paper. This phenomenon is often referred to as optical dot gain. Yule and Nielsen[26] have modeled this effect empirically through the use of an exponent, n. Also, it has been proposed[27] to use the n-value correction for improving the accuracy of the Neugebauer equation.[28] The Yule–Nielsen modification of the spectral Murray–Davies equation,[15] which is expected to improve the prediction accuracy, is as follows:

$$R_\lambda = \left[a_{\text{ink}} {R_{\lambda,\text{ink}}}^{1/n} + (1 - a_{\text{ink}}) {R_{\lambda,w}}^{1/n} \right]^n. \tag{4}$$

An n of 1.7 has been suggested for general conditions unless a priori knowledge about the particular ink and paper is available.[29] Alternatively, it is possible to determine the optimal n value and effective dot area optimizing Eq. 4 statistically. Because n is largely empirical, it can be further enhanced to vary as a function of physical dot area or wavelength. In the former case, extremely close fits result between the measured and estimated spectral reflectance factors in monochrome color ramps. However, it is impossible to extend to a multicolor print because a single n-value for the reflectance of the paper and for the shoulder of the right side term of Eq. 4 cannot be determined under this assumption. The wavelength enhancement can be readily applied as expressed in Eq. 5.

$$\begin{aligned}
R_\lambda = (&a_c {R_{\lambda,c}}^{1/n_\lambda} + a_m {R_{\lambda,m}}^{1/n_\lambda} + a_y {R_{\lambda,y}}^{1/n_\lambda} + a_k {R_{\lambda,k}}^{1/n_\lambda}\\
&+ a_r {R_{\lambda,r}}^{1/n_\lambda} + a_g {R_{\lambda,g}}^{1/n_\lambda} + a_b {R_{\lambda,b}}^{1/n_\lambda} + a_w {R_{\lambda,w}}^{1/n_\lambda})^{n_\lambda}.
\end{aligned} \tag{5}$$

Because, at most, four colors are observable as defined by the halftone algorithm, Eq. 5 is rewritten as follows:

$$R_\lambda = \left(a_k {R_{\lambda,k}}^{1/n_\lambda} + a_P {R_{\lambda,p}}^{1/n_\lambda} + a_s {R_{\lambda,s}}^{1/n_\lambda} + a_w {R_{\lambda,w}}^{1/n_\lambda} \right)^{n_\lambda}, \tag{6}$$

where subscript p and s indicate primary (C, M, or Ye) and secondary (R, G, or B) colors, respectively.

It is necessary to estimate n-values (n_λ) and effective dot areas (a_i) for predicting the printed reflectance factors using the model described by Eq. 6. It was first assumed that the dot areas equaled the theoretical dot areas. Then, n_λ was optimized for each wavelength using the Simplex nonlinear optimization method of SYSTAT[30] with sum-of-squares reflectance error of all colors of the modeling target as the minimization function. The n_λ values are plotted in Fig. 2. Second, the dot area in Eq. 6 was optimized for each color of the modeling target by linear optimization with sum-of-squares spectral error as the minimization function. These statistically derived dot areas are shown in Fig. 3 as data points. Figure 4 shows a reconstruction result of the spectral reflectance factor of the magenta ramp using Eq. 6 and values of optimized n_λ and dot area. The relationships between theoretical dot areas (defined via the halftoning algorithm) and effective dot areas (defined by the model coefficient for each linear optimization) for each color type were described using fourth-order poly-

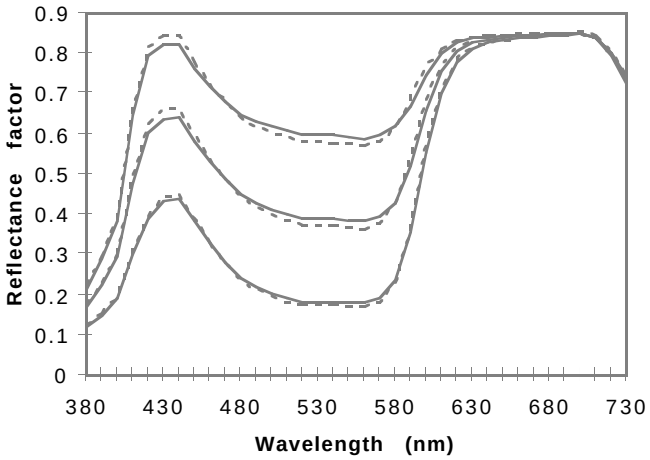

Figure 4. Spectral reflectance curves of magenta ramp measured (dashed line) and predicted (solid line) based on Eq. (6).

nomial equations (Eq. 7) and shown in Fig. 3 as lines. This nonlinearity was expected and is often referred to as mechanical dot gain. Figure 3 also shows that the secondaries had increased dot gain in comparison to the primaries, presumably due to wetting of the paper. Although the use of one-dimensional look-up tables to describe the nonlinearity is more common and will result in improved accuracy,[31] they can lead to adverse effects when inverting the model numerically. This will be described in greater detail.

$$f_i(a_i) = k_{4,i}{a_i}^4 + k_{3,i}{a_i}^3 + k_{2,i}{a_i}^2 + k_{1,i}a_i + k_{0,i}. \quad (7)$$

Following the flowchart shown in Fig. 5, colorimetric coordinates can be estimated from digital signal values. This flow consisted of (1) converting red, green, and blue digital counts to theoretical dot areas of each color type using the dot-on-dot halftone and the 100% GCR algorithms, (2) converting theoretical dot areas of each color type to effective dot areas using the polynomial equations, (3) using the Yule–Nielsen modified Murray–Davies equation, Eq. 6, to estimate spectral reflectance factor, and (4) calculating colorimetric coordinates.

The model effectiveness was evaluated by analyzing the verification target. The average total color difference between measured and predicted colors in CIELAB was 4.2 with a maximum of 11.7. The histogram of color differences and projection vector diagrams from measured to predicted colors in the a^*b^* and the $L^*C^*_{ab}$ planes are shown in Figs. 6 and 7, respectively.

Omatsu Model. A model that can predict reproduced reflectance factor for a three-color dot-on-dot printer has been suggested by Omatsu et al.[32] This model considers the scattering effect of the light within the paper. A Gaussian function is hypothesized to model the point spread function of the scattered light within the paper. This results in Eq. 8.

$$\begin{aligned} R = &\left\{a_k {R_k}^{1/2} + a_s {R_s}^{1/2} + a_p {R_p}^{1/2} + a_w {R_w}^{1/2}\right\}^2 \\ &+2\exp(-\pi^2\sigma^2/L^2)\{({R_s}^{1/2} - {R_k}^{1/2})\sin(\pi a_k) \\ &+({R_p}^{1/2} - {R_s}^{1/2})\sin\left(\pi(a_k + a_s)\right) \\ &+({R_w}^{1/2} - {R_p}^{1/2})\sin\left(\pi(a_k + a_s + a_p)\right)\}^2/\pi^2, \end{aligned} \quad (8)$$

where σ is a length of the scattered light, L is the screen resolution of a printer, and subscripts p and s indicate primary and secondary. If σ is 0, Eq. 8 reduces to the Neugebauer equation, and if σ is infinity, it reduces[32] to the Yule–Nielsen equation where n equals 2.0. Coefficient σ was defined as a single value in the original model. In similar fashion to n, σ is extended to vary as a function of wavelength because light scattering is, in general, wavelength dependent. It is difficult to measure coefficient σ_λ directly. However, it is possible to optimize these coefficients for the measured colors of the printer statistically. In this case, a single coefficient α_λ was considered instead of elements of the exponential function in Eq. 8. Therefore, it was not necessary to measure the screen resolution L directly. Accordingly, Eq. 8 reduces to Eq. 9.

$$\begin{aligned} R_\lambda = &\left\{a_k {R_{\lambda,k}}^{1/2} + a_s {R_{\lambda,s}}^{1/2} + a_p {R_{\lambda,p}}^{1/2} + a_w {R_{\lambda,w}}^{1/2}\right\}^2 \\ &+2\exp(\alpha_\lambda)\{({R_{\lambda,s}}^{1/2} - {R_{\lambda,k}}^{1/2})\sin(\pi a_k) \\ &+({R_{\lambda,p}}^{1/2} - {R_{\lambda,s}}^{1/2})\sin\left(\pi(a_k + a_s)\right) \\ &+({R_{\lambda,w}}^{1/2} - {R_{\lambda,p}}^{1/2})\sin\left(\pi(a_k + a_s + a_p)\right)\}^2/\pi^2 \end{aligned} \quad (9)$$

Optimizing the coefficients in the Omatsu model was performed in a similar fashion to optimizing the coefficients in the Murray–Davies–Yule–Nielsen model. It was first assumed that the effective dot areas were equal to the theoretical dot areas. Then the α_λ was estimated for each wavelength in a fashion similar to that used to estimate n_λ. The optimized α_λ values are plotted in Fig. 8. With defined α_λ values, the effective dot areas were estimated for each sample from the modeling target minimizing sum-of-squares spectral reflectance factor error. The resulting effective dot areas are shown in Fig. 9 as data points. Figure 10 shows reconstructed spectral reflectance curves of the magenta ramp using this model. The relationships between theoretical dot areas and effective dot areas were described using sixth-order polynomial equations (Eq. 10) and shown in Fig. 9 as lines.

$$\begin{aligned} &f_i(a_i) = \\ &k_{6,i}{a_i}^6 + k_{5,i}{a_i}^5 + k_{4,i}{a_i}^4 + k_{3,i}{a_i}^3 + k_{2,i}{a_i}^2 + k_{1,i}a_i + k_{0,i}. \end{aligned} \quad (10)$$

The effectiveness for the Omatsu model was also evaluated using the verification target. The average color difference was $3.9\Delta E^*_{ab}$ with a maximum of $11.4\Delta E^*_{ab}$. The ΔE^*_{ab} histogram and the a^*b^* and the $L^*C^*_{ab}$ projection vector diagrams are shown in Figs. 11 and 12, respectively.

Discussion. The n_λ and σ_λ coefficients should be smooth functions; however, abrupt changes were observed in both coefficients, as shown in Figs. 2 and 8. It seems that these changes correspond to steep portions of the spectral reflectance factors of the primary and secondary inks. Figure 13 shows the average reflectance factor of the modeling data set. It is obvious that a similar trend is observed. Jagged functions can often result because each data point is based on an independent optimization. The jaggedness can be minimized by imposing a constraint, often based on the first derivative of the spectral reflectance factor. It seems that these kinds of fluctuations of the average reflectance factor affected the n_λ and σ_λ coefficients.

Color difference statistics of the two models are compared with one another in Table I. The average color differences of the two models are very similar in spite of using

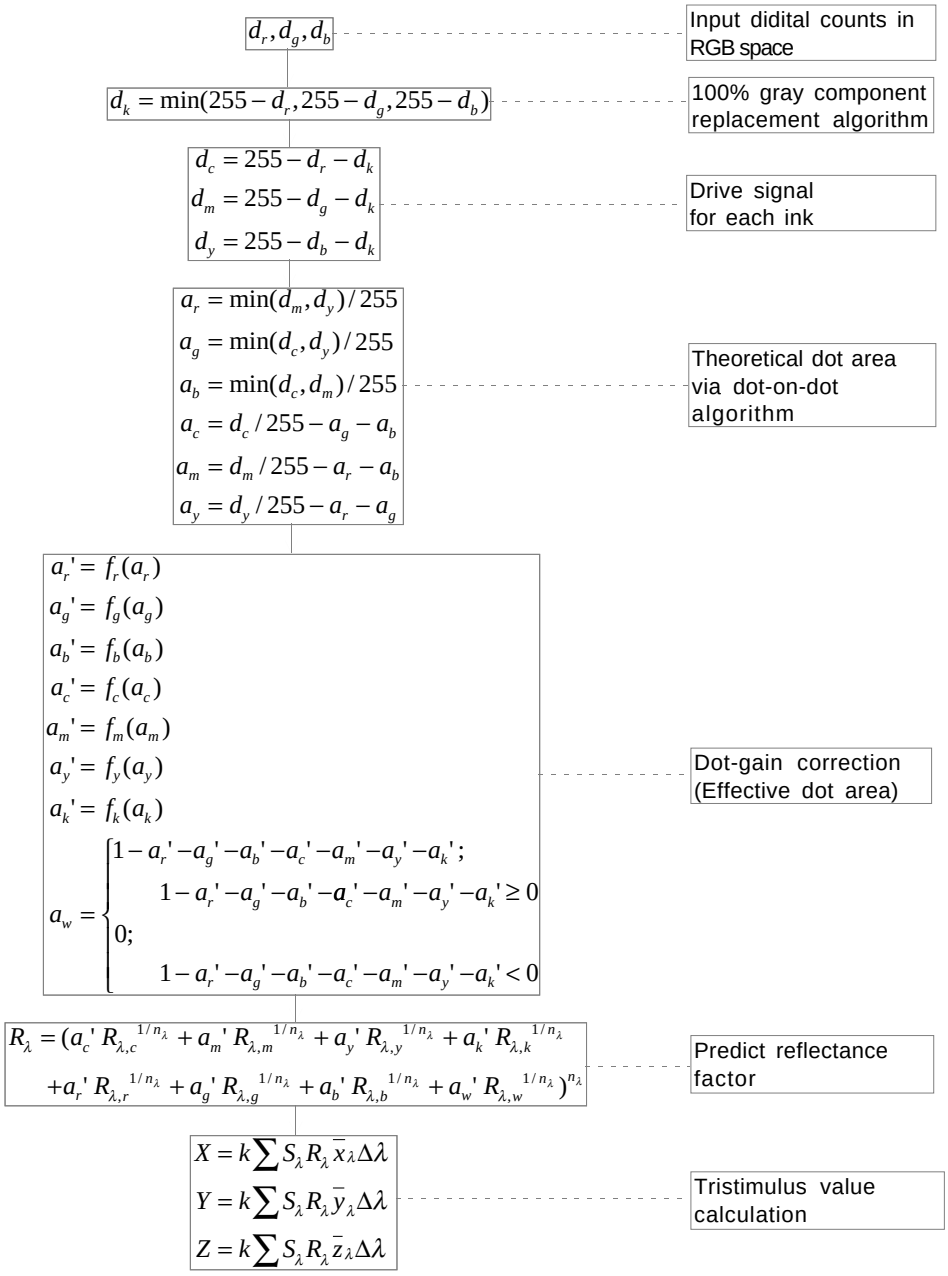

Figure 5. Forward model flowchart of prediction model for dot-on-dot and 100% GCR algorithm using spectral Yule–Nielsen modified Murray–Davies equation.

different model theories; the trends shown in Figs. 7 and 12 are similar to each other. Moreover, the maximum color difference for the models correspond to the same sample of the verification target. Figure 14 shows the three spectral reflectance factor curves of this sample and its estimates. The predicted curves are almost the same; however, the measured data are very different. It is possible that the halftoning algorithm described by Eqs. 1 and 2 is not strictly adhered to. Manufacturers often adjust particular colors due to color (e.g., hue shifts) or spatial (e.g., resolution and sharpness) artifacts. This was tested for the color shown in Fig. 14 and another color with different digital counts but yielding the identical dot area for the magenta ink. When both samples were viewed under a microscope, it was clear that the magenta dot areas were quite different. If the printer driver was optimized for certain colors, it would be impossible to account for this in a generalized model. It is possible that the verification target contained only a few of these optimized colors. Alternatively, the poor result may be due to random error, although this seems unlikely.

These two models have similar predicting performances according to Table I. In comparison between Eqs. 6 and 9, it is expected that the computational loads of Eq. 6 and the first term of Eq. 9 are almost the same. It is obvious that the Omatsu model (Eq. 9) needs more computational time, a disadvantage when building device profiles. Moreover, the spectral Yule–Nielsen equation has some extension ability for random-dot halftone printers. For example, this modification can be extended to the well-known Neugebauer equation.[28] Conversely, it is difficult to extend the Omatsu equation for random dot patterns because the model is based on the assumption of a fixed dot-on-dot pattern. It does not allow for the existence of more than one primary, secondary, and tertiary color present. Because of these reasons, the spectral Murray–Davies equation

TABLE I. Color Difference Statistics for Predicted Printed Colors by Two Models

Model	Statistics	Modeling target	Verification target
Spectral	Average ΔE^*ab	2.3	4.2
Yule–Nielson Model	Maximum ΔE^*ab	5.1	11.7
	Standard deviation	1.3	2.5
	Average ΔE^*ab	2.1	3.9
Omatsu Model	Maximum ΔE^*ab	5.0	11.4
	Standard deviation	1.5	2.3

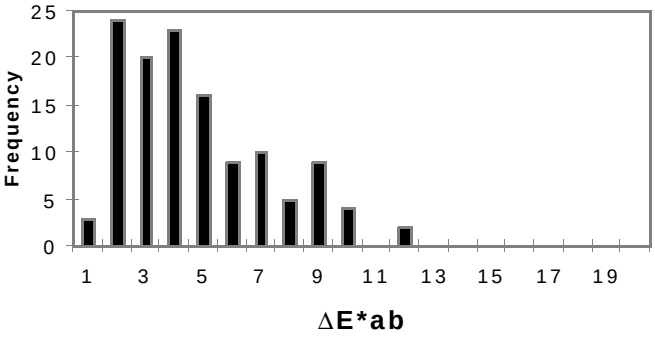

Figure 6. Color difference histogram of model performance based on Eq. 6.

modified by the Yule–Nielsen spectral-n-values correction was selected as the model for building a device profile.

Scanner Forward Model

Several methods for building scanner device profiles have been described in the literature: polynomial regression methods,[7,33] look-up-table and interpolation methods,[34] and spectral reconstruction methods.[8–12] Although the last technique is preferred for drum scanners, when applied to the scanner used in this research, the results were unacceptable.[12] As a consequence, a polynomial regression model was used. Generally, this method is separated into two stages.[6,7,33] The first stage characterizes an expected nonlinear relationship between device signals and luminance factor of a neutral target. However, because the gray scale of the Kodak Ektacolor Q-60R1 was not completely neutral, an alternate approach was taken. In this case, the device signals of each channel were related mathematically with the corresponding tristimulus value of the gray scale. The red channel was related to tristimulus X, green to tristimulus Y, and blue to tristimulus Z of the gray-scale samples. Equation 11 was used to characterize this nonlinear relationship:

$$f_i(d_i) = (\xi_i \frac{d_i}{255} + \eta_i)^{\gamma_i} + \zeta_i, \qquad (11)$$

where d is digital count, subscript i indicates a channel, and ξ, η, ζ, and γ are model coefficients. Each coefficient was determined for each channel of the scanner individually using nonlinear optimization where the objective function minimized the sum-of-squared errors of the cube root of tristimulus values of the gray steps of the Q-60R1. This objective function greatly improves the correlation to perceived differences by incorporating the cube-root function used in the CIELAB equations.[33]

The second stage transforms the linearized drive signals to approximations of tristimulus values.[7,33] This step can be thought of as color correction. Based on previous research with this scanner,[33] a 3×9 color-correction matrix was hypothesized consisting of linear, squared, and covariance terms shown by Eq. 12. The matrix coefficients were estimated using nonlinear optimization with the same nonlinear objective function used to characterize the scanner's tone reproduction. The matrix resulted in an average ΔE^*_{ab} of 2.1 with a maximum ΔE^*_{ab} of 8.1 for the Q-60R1. This is a reasonable result given that the system spectral responsivities of the scanner are very different from CIE 1931 color matching functions weighted by illuminant D_{65}.

The combination of Eqs. 11 and 12 was used as the scanner device profile that transformed digital representations of Ektacolor images to approximate tristimulus values for the 1931 CIE standard observer and illuminant D_{65}. The ΔE^*_{ab} histogram and the a^*b^* and the $L^*C^*_{ab}$ projection vectors are shown in Figs. 15 and 16, respectively.

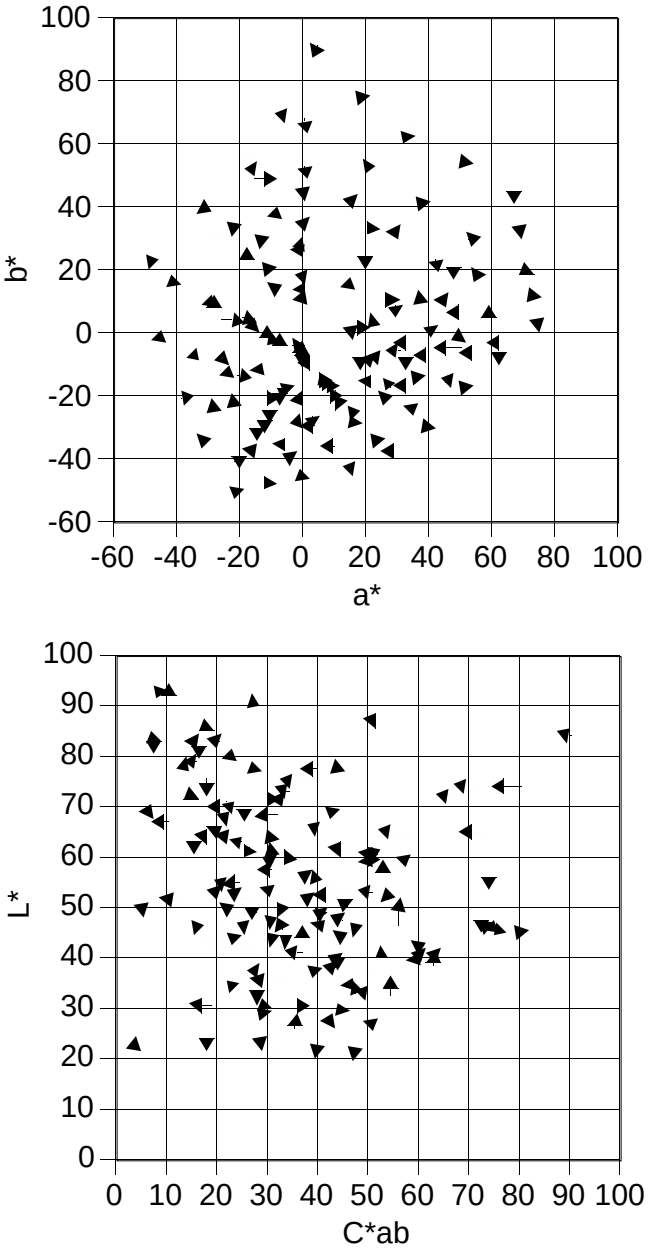

Figure 7. Error vectors of predicted colors based on Eq. 6 for the verification target. Vector tail locates the measured coordinate; vector head locates the predicted coordinate.

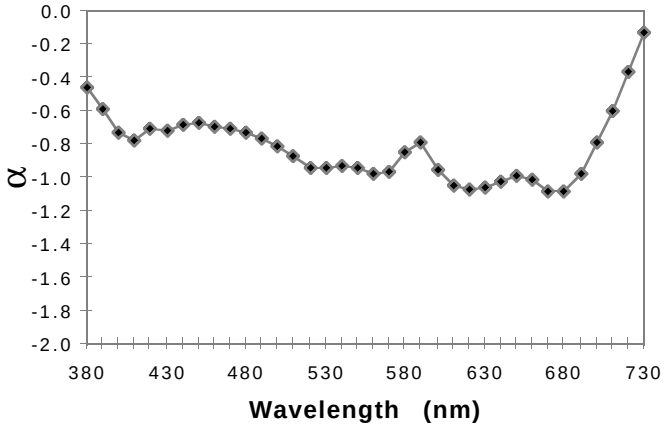

Figure 8. Optimized α-values in Eq. 9 as a function of wavelength.

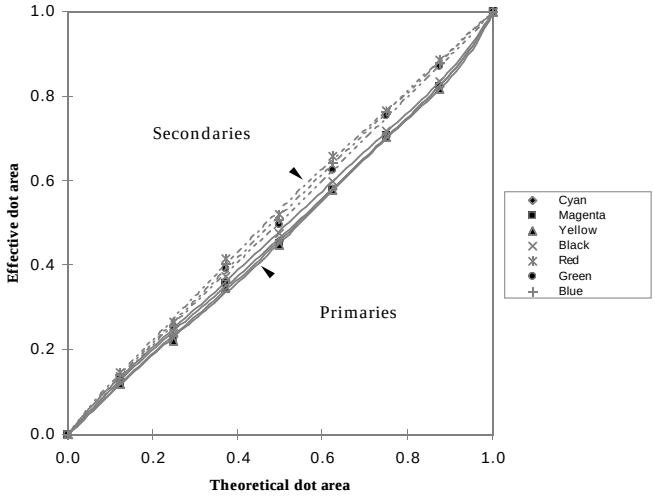

Figure 9. Relationship between theoretical dot area and statistically derived effective dot area. Lines joining data were derived using forth-order polynomial models.

$$\begin{bmatrix} X \\ Y \\ Z \end{bmatrix} = \begin{bmatrix} a_{11}a_{12}\ldots a_{19} \\ a_{21}a_{21}\ldots a_{29} \\ a_{31}a_{31}\ldots a_{39} \end{bmatrix} \begin{bmatrix} R \\ G \\ B \\ R\cdot G \\ G\cdot B \\ B\cdot R \\ R\cdot R \\ G\cdot G \\ B\cdot B \end{bmatrix}. \quad (12)$$

Building the Color-Management Module

The color-management module (CMM) developed in this research consisted of concatenating the scanner and printer device profiles and a rudimentary color gamut mapping into a 33^3 CLUT. Cubical linear interpolation was used to estimate values between the nodes.[35] Ordinarily, color appearance is also included in the CMM.[36,37] However, both the original and reproduced images are reflection prints; in this case, they will have identical viewing conditions. As a consequence, color appearance matching reduces to tristimulus

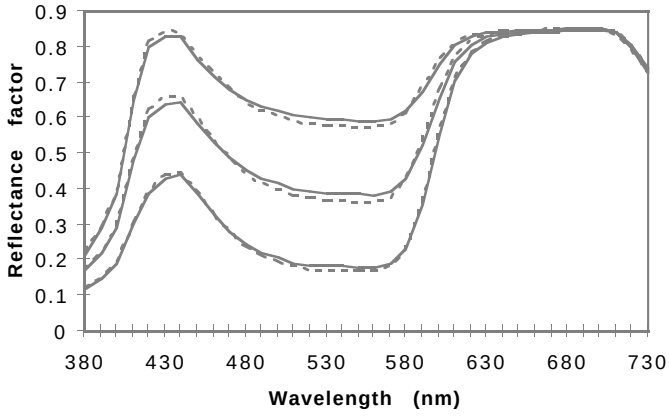

Figure 10. Spectral reflectance curves of magenta ramp measured (dashed line) and predicted (solid line) based on Eq. 11.

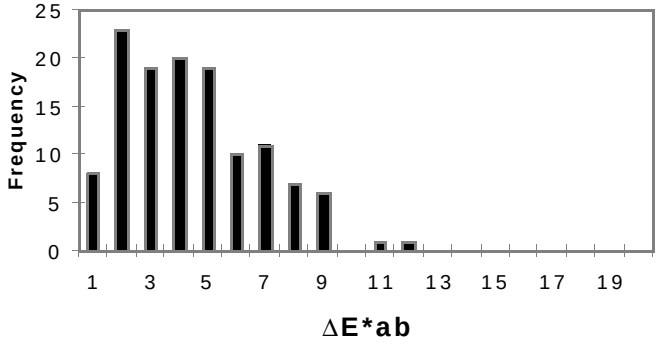

Figure 11. Color difference histogram of model performance based on Eq. 11.

matching, obviating the need for an explicit color appearance model except for gamut mapping.

The number of nodes of the CLUT, the orientation of the nodes within a three-dimensional space, and the type of subspace volume all affect the interpolation and extrapolation accuracy.[2] Because these issues were outside the scope of this research, a large CLUT was used that, hopefully, minimized these artifacts.

Visual and colorimetric evaluations indicated that the ink-jet color gamut was considerably smaller than the photographic color gamut, particularly in the lightness dimension. This is exemplified in Figs. 7 and 16 in the $L^*C^*_{ab}$ plots; the minimum L^* for the ink-jet printer was around 20 while the minimum lightness for the photographic paper was about 5. There was also a noticeable difference in the color of each substrate. The differences in the chromatic dimensions for these two devices, as shown in the b^*a^* plots, were modest. For the current research goals, the following gamut-mapping strategy was employed. More elaborate methods are described in Refs. 39 to 45.

The RLAB color appearance model[46] was used to define the color appearances of the two media according to Eq. 13:

$$\begin{aligned} L^R &= 100(Y/100)^{1/2.3}, \\ a^R &= 430[(X/100)^{1/2.3} - (Y/100)^{1/2.3}], \\ b^R &= 170[(Y/100)^{1/2.3} - (Z/100)^{1/2.3}], \end{aligned} \quad (13)$$

where the exponent was defined based on average-surround viewing, typical of hardcopy. RLAB was selected due to its computational simplicity and improved accuracy in

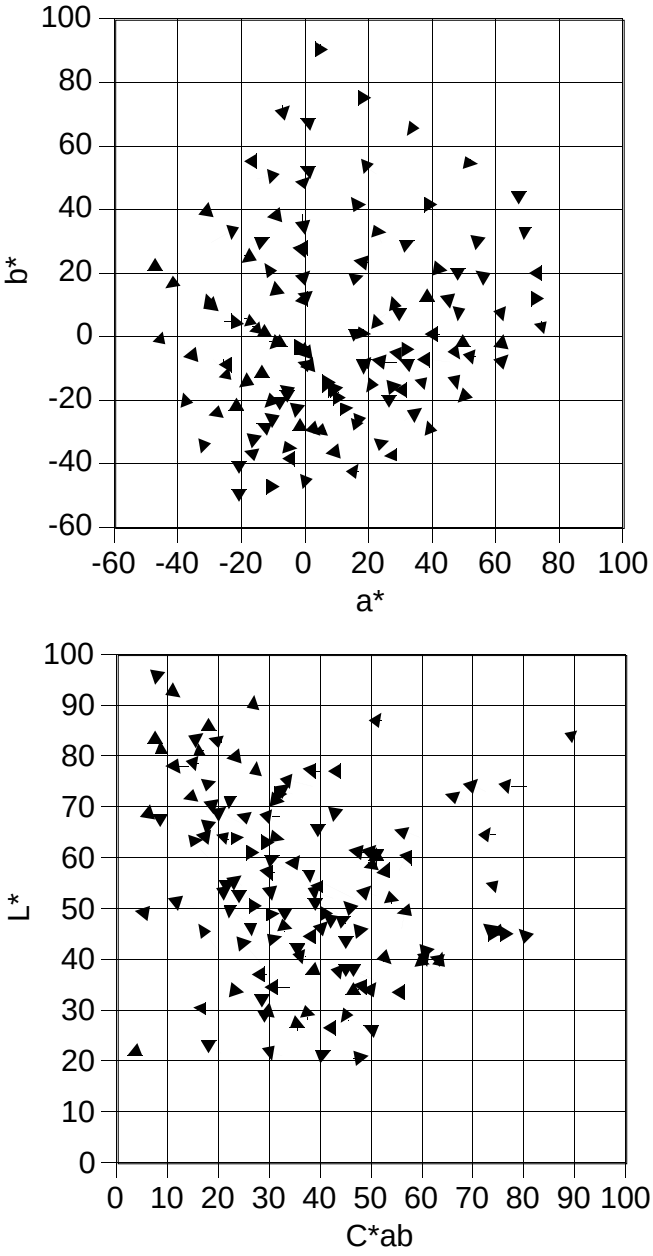

Figure 12. Error vectors of predicted colors based on Eq. 11 for the verification target. Vector tail locates the measured coordinate; vector head locates the predicted coordinates.

defining color appearance in comparison to CIELAB. The white and black points of the two media are shown in Table II. Because of these large differences and our research goal to evaluate colorimetric accuracy, the color gamut of the photographic target was linearly compressed using Eq. 14. The compressed data were used to redefine the "original" colorimetric coordinates of this medium. Residual differences in color gamut were accounted for during the printer inversion by employing minimum ΔE^*_{ab} clipping.

$$L^R_{\text{destination}} = \begin{cases} 24.0; & L^R_{\text{original}} < 6.4 \\ 0.85L^R_{\text{original}} + 18.35; & 6.4 \le L^R_{\text{original}} \le 89.0 \\ 94.0; & L^R_{\text{original}} > 89.0, \end{cases}$$

$$a^R_{\text{destination}} = a^R_{\text{original}},$$

$$b^R_{\text{destination}} = b^R_{\text{original}}. \qquad (14)$$

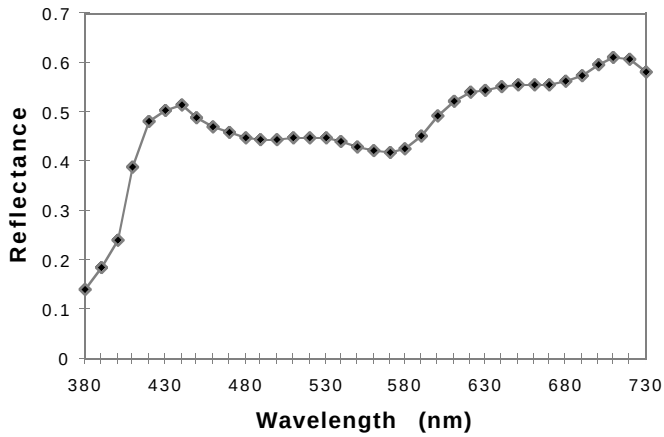

Figure 13. Averaged reflectance factor of 57 modeling samples.

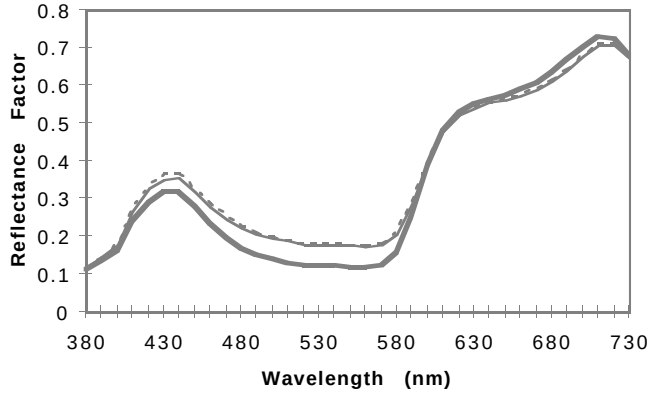

Figure 14. Reflectance curves of measured (thick line) and predicted by Yule–Nielsen model (thin line) and by Omatsu model (dashed line). These predicted curves gave maximum color differences for the verification target.

TABLE II. Maximum and Minimum Lightness of Original and Printer

	$L^R_{\max}$	$L^R_{\min}$
Original (Q-60R1)	89.0	6.4
StyleWriter Pro	94.0	24.0

Inverse Printer Forward Model. It is difficult to derive an inverse function of the forward printer model analytically because the model equations are impossible to solve mathematically. Therefore, it is necessary to use an iterative method to invert the forward printer model. Two iteration methods were evaluated, the Newton-Raphson and the Simplex methods.

Newton–Raphson Method. Suppose that the first approximation to finding a root of an equation of the form $f(x) = 0$ is x_n. An improved approximation, x_{n+1}, is given by Eq. 15 according to the Newton–Raphson method[47] where $f'(x_n)$ is the derivative of $f(x_n)$. The same procedure is repeated to achieve a better approximation and the iteration continues until the function value becomes less than some prescribed small value.

$$x_{n+1} = x_n + \Delta x = x_n - \frac{f(x_n)}{f'(x_n)}. \qquad (15)$$

Expanding the Newton–Raphson method to the three-dimensional color space,[48] an application for the inversion

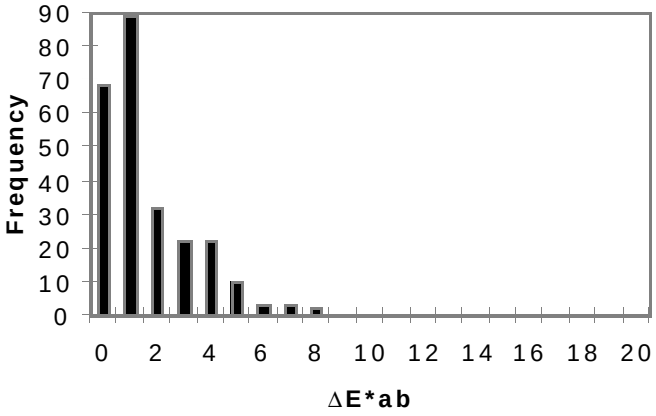

Figure 15. Color difference histogram of model performance for the scanner model based on Eqs. 17 and 19.

of the printer forward model [$f_x(d_r,d_g,d_b)$] is described below. The tristimulus values corresponding to the initial digital counts of d_{r0}, d_{g0}, and d_{b0} are approximated as X_0, Y_0, and Z_0. The small change of tristimulus value ΔX according to the small changes of digital counts Δd_r, Δd_g, and Δd_b is expressed in Eq. 16, similar in form to Eq. 15.

$$\begin{aligned} X_0 + \Delta X &= fx(d_{r0} + \Delta d_r, d_{g0} + \Delta d_g, d_{b0} + \Delta d_b), \\ &= fx(d_{r0}, d_{g0}, d_{b0}) + \Delta d_r \partial fx / \partial d_r \\ &\quad + \Delta d_g \partial fx / \partial d_g + \Delta d_b \partial fx / \partial d_b, \\ &= X_0 + \Delta d_r \partial X / \partial d_r + \Delta d_g \partial X / \partial d_g + \Delta d_b \partial X / \partial d_b. \end{aligned} \tag{16}$$

Tristimulus Y and Z values are obtained in similar fashion. These relationships are expressed in a matrix representation as follows:

$$\begin{pmatrix} \Delta X \\ \Delta Y \\ \Delta Z \end{pmatrix} = \begin{pmatrix} \partial X / \partial d_r & \partial X / \partial d_g & \partial X / \partial d_b \\ \partial Y / \partial d_r & \partial Y / \partial d_g & \partial Y / \partial d_b \\ \partial Z / \partial d_r & \partial Z / \partial d_g & \partial Z / \partial d_b \end{pmatrix} \begin{pmatrix} \Delta d_r \\ \Delta d_g \\ \Delta d_b \end{pmatrix}. \tag{17}$$

By multiplying the inverse matrix of the first right side term of Eq. 17, Eq. 18 is obtained.

$$\begin{pmatrix} \Delta d_r \\ \Delta d_g \\ \Delta d_b \end{pmatrix} = \begin{pmatrix} \partial X / \partial d_r & \partial X / \partial d_g & \partial X / \partial d_b \\ \partial Y / \partial d_r & \partial Y / \partial d_g & \partial Y / \partial d_b \\ \partial Z / \partial d_r & \partial Z / \partial d_g & \partial Z / \partial d_b \end{pmatrix}^{-1} \begin{pmatrix} \Delta X \\ \Delta Y \\ \Delta Z \end{pmatrix}. \tag{18}$$

The digital counts for correction Δd_r, Δd_g, and Δd_b are calculated from the differences between the target tristimulus values and their approximations (ΔX, ΔY, and ΔZ) using Eq. 18. The corrected digital counts d_{r1}, d_{g1}, and d_{b1} in Eq. 19 would result in a better approximation. The same procedure is repeated until the color difference becomes less than a defined tolerance.

$$\begin{aligned} d_{r1} &= d_{r0} + \Delta d_r, \\ d_{g1} &= d_{g0} + \Delta d_g, \\ d_{b1} &= d_{b0} + \Delta d_b. \end{aligned} \tag{19}$$

Ideally, the partial derivatives are calculated from the forward models analytically.[49,50] However, because the forward printer model was complicated, it is more efficient

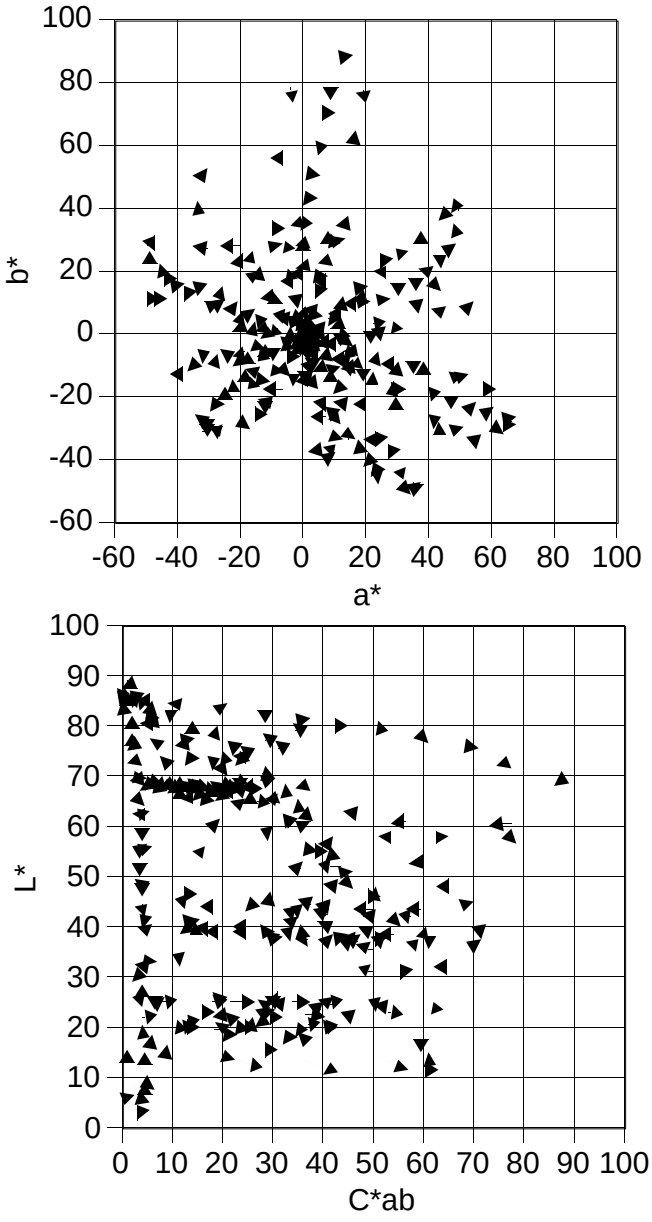

Figure 16. Error vectors of regression scanner model for Q-60R1. Vector tail locates the measured coordinates; vector head locates the predicted coordinates.

to calculate the partial derivatives numerically. To implement the numerical approximation it was necessary to extrapolate the input digital counts beyond the usual 0 to 255 range to avoid a zero determinant when calculating an inverse matrix. The polynomial equations, which expressed the relationship between theoretical dot areas and effective dot areas in the printer forward models, were used in the Newton–Raphson method to obtain a reasonable extrapolation. In addition, it was easy for the polynomial equations to set small changes of digital counts (Δd_r, Δd_g, Δd_b). For these two reasons, polynomial equations were preferred to one-dimensional look-up tables.

The initial digital counts for the iteration were set[49] to the midpoint of the input space $d_{r0} = d_{g0} = d_{b0} = 128$. Small digital count changes for calculating the partial derivatives numerically were set to $\Delta d_r = \Delta d_g = \Delta d_b = 1.0$ because the minimum change in digital counts is one unit. The digital count range was not limited. The tolerable color difference that was the condition for stopping iteration

was set to 1.0 ΔE^*_{ab}. The final digital counts were clipped to 0 and 255 if beyond the normal operating range.

In testing the above method, many in-gamut colors did not converge: they either diverged to a gamut surface or oscillated between two values. Limitations using the Newton–Raphson method are well known. To minimize problems of oscillation, the minimum change in digital count (Δd_r, Δd_g, Δd_b) was reduced from unity to 0.1. To improve convergence, Eq. 20 was used[51] instead of Eq. 15. According to this correction, ω is set to 1 at the first step. If no improvement occurs in the function result, ω is reduced to 1/2. If no improvement again, ω is reduced to 1/4, etc. This correction is continued until the function result improves.

$$x_{n+1} = x_n - \omega \frac{f(x_n)}{f'(x_n)} \quad 0 < \omega \leq 1 \tag{20}$$

The flowchart of a computer program of the Newton–Raphson method implemented in this research is shown in Fig. 17.

Oscillations and divergences for most colors were suppressed by the ω correction and reduced step size, though at the cost of increased computational time. Colors either at the boundary or outside of the gamut still resulted in convergence problems.

Simplex Method. The Simplex method is a direct search method. Because it does not rely on calculating derivatives, convergence problems encountered using the Newton–Raphson method are not expected to occur. However, this reduction of information tends to increase the number of iterations to achieve convergence. (Note that adding ω also increases the number of iterations such that the two methods require about the same amount of total computational time.) Using four operations (reflection, expansion, contraction, and reduction), the minimum point of a function is obtained.[51,52]

In this research, initial digital counts were first set to $d_{r0} = d_{g0} = d_{b0} = 128$ as employed using Newton–Raphson. However, the iteration often stopped despite large residual color differences, a result of local minima. Thus, choosing the initial values is very important using the Simplex method. The initial digital counts that resulted in the fewest problems with local minima were: $d_{r0} = 255X/X_n$, $d_{g0} = 255Y/Y_n$, and $d_g = 255Z/Z_n$ where X, Y, and Z were the tristimulus values of the target color and X_n, Y_n, and Z_n, were the illuminant tristimulus values. Therefore, the initial simplex was defined[51] as follows:

$$\begin{aligned}
\mathbf{P}_0 &= [255X/X_n, 255Y/Y_n, 255Z/Z_n], \\
\mathbf{P}_1 &= [255X/X_n + s_1, 255Y/Y_n + cs_2, 255Z/Z_n + cs_3], \\
\mathbf{P}_2 &= [255X/X_n + cs_1, 255Y/Y_n + s_2, 255Z/Z_n + cs_3], \\
\mathbf{P}_3 &= [255X/X_n + cs_1, 255Y/Y_n + cs_2, 255Z/Z_n + s_3],
\end{aligned} \tag{21}$$

where

$$c = 1/(\sqrt{n+1} + 2), \quad n = 3,$$
$$s_i = \text{scale factors}.$$

The CIELAB color difference between the target color and its prediction defined the minimization function. Also, the best and worst simplexes were defined as sets of values obtained from the minimum and the maximum results of the minimization function among given simplexes, respectively. Any of the following conditions resulted in termination: (1) if the differences between element values of the best and the worst simplexes were less than 0.5 digital value, (2) if the color differences for both best and worst simplexes were the same, and (3) if the number of iterations exceeded a defined maximum iteration number. When one of three termination conditions was detected and the residual color difference from the final simplex was still larger than the defined tolerance of 1.0 ΔE^*_{ab}, the calculation resumed using the final simplex from the first calculation as an initial simplex to avoid termination at a local minimum. This routine was very effective in converging at the true minimum. The following simplex coefficients were used as recommended by Kowalik and Osborn:[53] Reflection coefficient = 1.0, Expansion coefficient = 2.0, and Contraction coefficient = 0.5. These same values were also used successfully by Ohta for photographic systems.[54] The flowchart of the Simplex method used in this research is shown in Fig. 18.

The range of input digital counts was limited between 0 and 255 at the entrance of the printer forward model for obtaining an existing approximated root using a sawtooth function (Fig. 19). Although it is possible for the Simplex method to limit the range of input values before the printer model,[54] the range of digital counts in the simplex calculation was, instead, constrained by the sawtooth function. This function was extremely effective in ensuring convergence at the true minimum. If the input values are simply clipped and not extended by the sawtooth function, the calculation will terminate prematurely because no incremental improvement occurs.

The method worked well without oscillation and divergence problems. However, it took, on average, about 30 iterations for convergence without the recalculation routine.

System Evaluation. The forward scanner profile, gamut resizing, and inverse printer profile including gamut mapping were concatenated to form a single CLUT. Software developed by the RIT Research Corporation[35] was used to perform the three-dimensional cubical interpolation. This software was written as a plug-in filter for Adobe PhotoShop. Thus, image data, based on scans using the JX-610, were transformed to image files that when sent to the ink-jet printer, would result in colorimetric color reproduction. The colorimetric coordinates of the prints were measured spectrophotometrically to evaluate colorimetric accuracy. The largest CLUT available in this software package, 33^3, was used to minimize potential artifacts caused by the cubical sampling and deterioration of the profile near gamut boundaries. The corners of the input space RGB cube might be transformed to unexpected values because their corresponding colorimetric coordinates are outside of the printer gamut. In addition, colors that place a border between the outside and inside of the printer gamut might be transformed to unexpected points. Larger CLUTs result in fewer artifacts. Because both profiles are analytical in nature, it is straightforward to build a CLUT of any size.

The projected error vectors from the reproduced target colors of Q-60R1 are shown in Figs. 20 and 21 based on the Newton–Raphson and the Simplex methods, respectively. Reproduced colors with large color differences from target colors in Fig. 20 correspond to those in Fig. 21. It seemed that these colors were almost outside of the printer gamut. The directions of error vectors were very different and depended on the iteration method. According to the large-error target colors, reproduced colors from the Simplex method were located nearer to the target colors than those from the Newton–Raphson

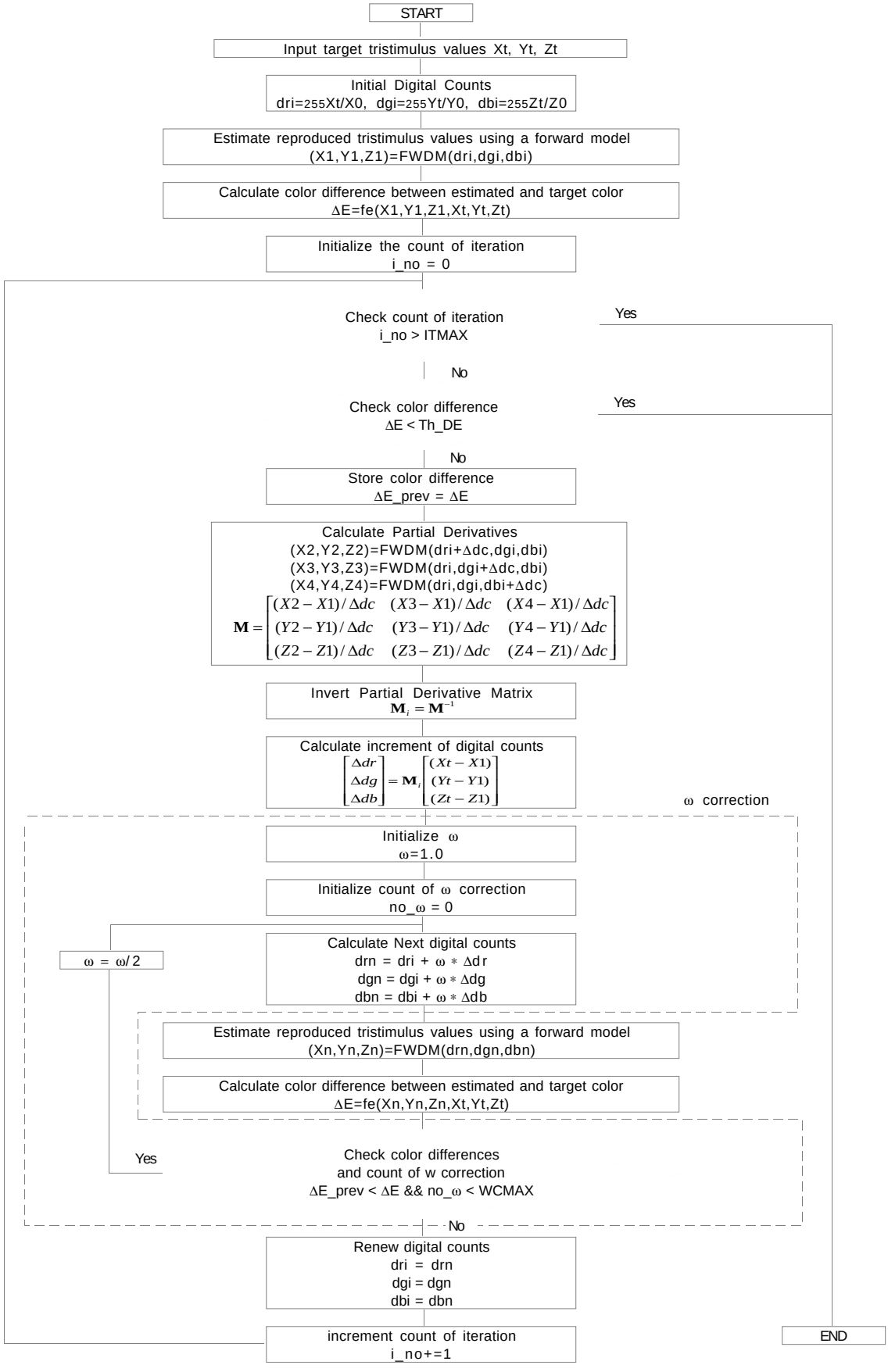

Figure 17. Program flowchart of iteration method for backward printer model using the Newton–Raphson, where Th_Δ*E* is tolerable color difference, ITMAX is the number of maximum iteration times, WCMAX is the number of maximum ω correction times, and FWMD is the printer forward model.

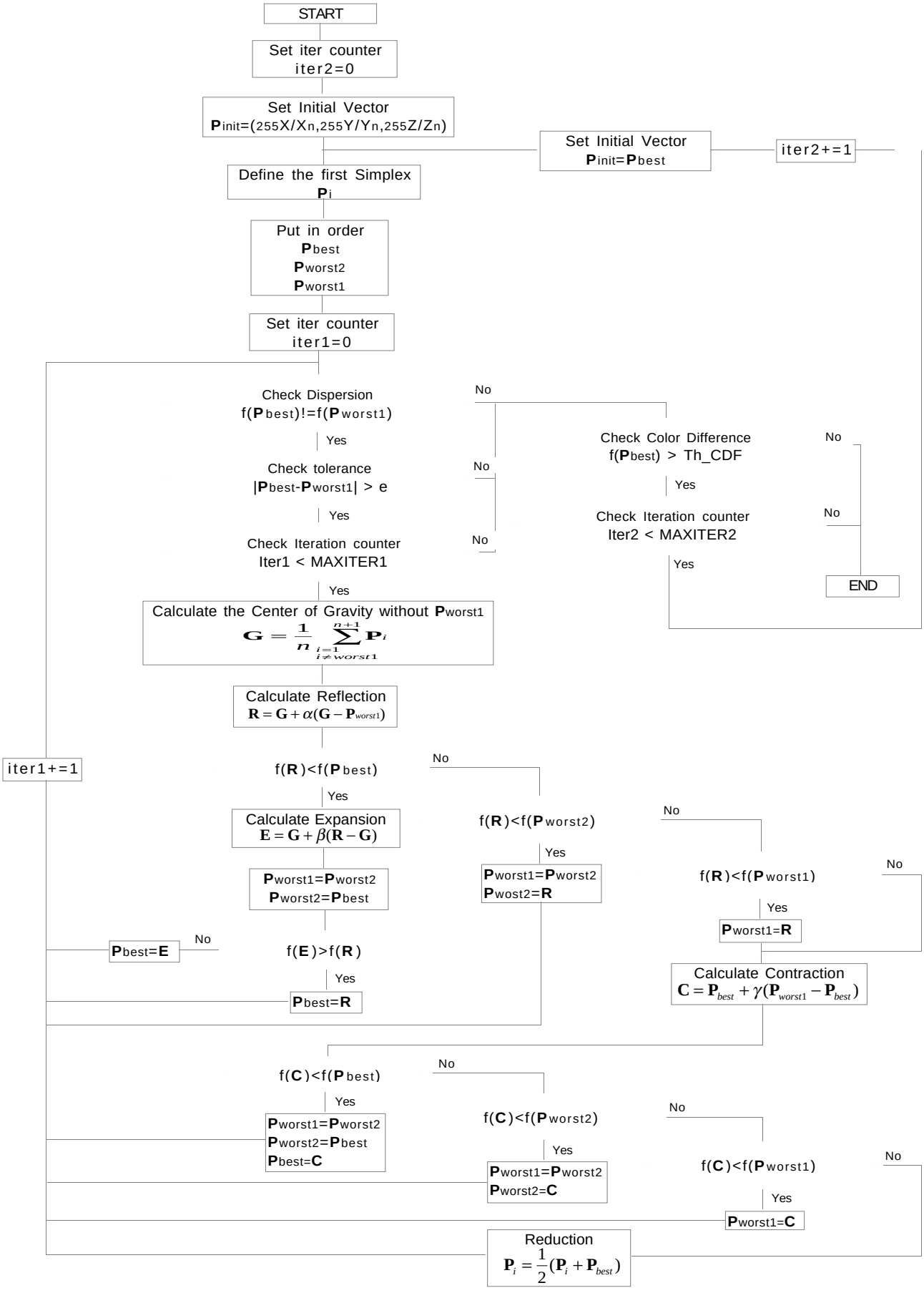

Figure 18. Program flowchart of iteration method for backward printer model using Simplex, where *f(P)* is the printer forward model.

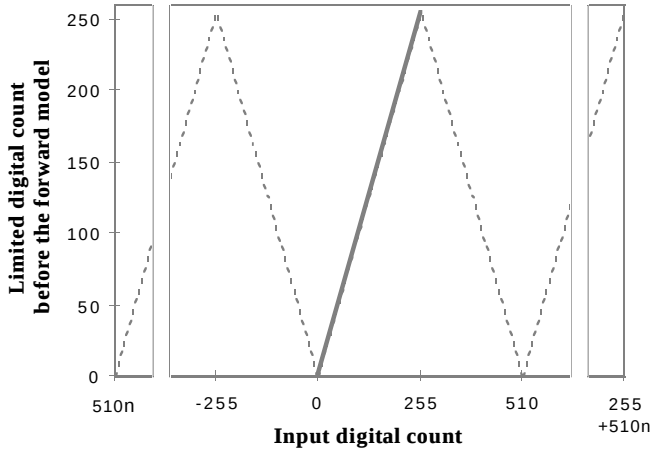

Figure 19. Limitation function using between input simplex and the forward model. Digital count of input simplex is not limited.

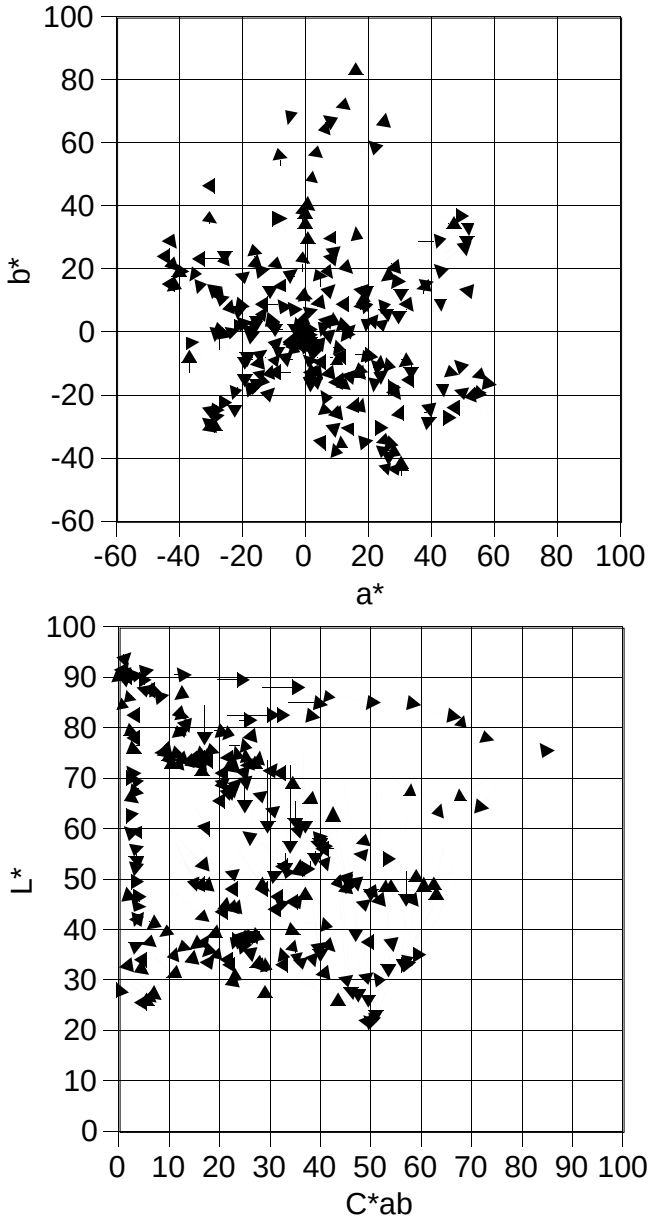

Figure 20. Error vectors of reproduced colors by concatenating device profile made by the Newton–Raphson iteration method. Vector tail locates target coordinate; vector tail locates reproduced coordinate.

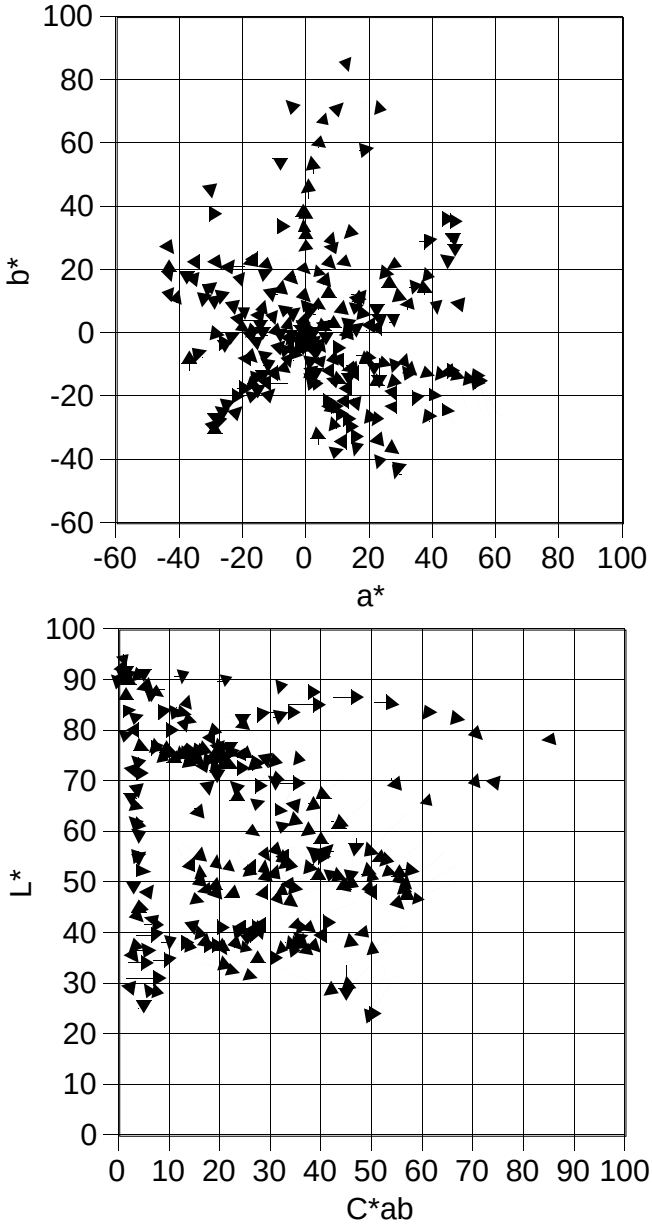

Figure 21. Error vectors of reproduced colors by concatenating device profile made by the Simplex iteration method. Vector tail locates target coordinate; vector tail locates reproduced coordinate.

method. The Simplex method can find true minima for colors near the edge or outside of the gamut, whereas the Newton–Raphson method could not. Color difference histograms between the target colors and their reproductions are shown in Fig. 22. Fig. 22(a) and 22(b) represent the Q-60R1 colors following lightness remapping. Figures 22(c) and 22(d) were constrained to include only common gamut colors. The color difference statistics are given in Table III. The Simplex method resulted in less errors than the Newton–Raphson method. It is also obvious that the substantive difference between the two methods occurred outside of the printer gamut. The Newton–Raphson method was unstable resulting in mapped colors at unexpected locations. Apparently, the usual limitations of the Newton–Raphson method are amplified beyond gamut boundaries preventing the accurate location of the printable color based on minimum ΔE^*_{ab} clipping. In particular, data extrapolation caused errors in calculating

TABLE III. Colorimetric Performance Statistics of Device Profiles

Targets and statistics		Iteration method	
		Newton–Raphson	Simplex
All target	Avg. ΔE^*ab	8.9	5.9
Max. ΔE^*ab		32.9	17.8
Std. dev.		5.6	3.5
Inside gamut target	Avg. ΔE^*ab	7.0	4.9
Max. ΔE^*ab		15.9	12.4
Std. dev.		3.4	2.6

the partial derivatives that were not overcome by limiting the digital range between 0 and 255. The Simplex method did not appear to suffer from this limitation. The sawtooth function improved convergence to the true solution. For common gamut colors, the two methods were similar in performance.

The system performance can be quantified by calculating the average color difference of the CLUT. Average ΔE^*_{ab} values below about 2.5 are below visual threshold[55] while average values below about 6 result in acceptable color reproduction accuracy for pictorial images.[55,56] The average of all the colors was 5.9 while the average error for common gamut colors was 4.9 when using the Simplex algorithm. Thus, the CLUT based on the Simplex method would yield acceptable color reproduction accuracy for applications appropriate to the use of ink-jet printers.

Conclusions

A color-management module or CMM was developed and tested for a desktop color system consisting of a flat-bed scanner imaging photographic reflection prints and an ink-jet printer using coated ink-jet paper. The first step was to develop forward models for the scanner and printer. The second step was to define a gamut mapping strategy. The third step was to concatenate the scanner forward model, gamut mapping strategy, and an inverse model of the printer into a 33^3 CLUT, thereby defining the CMM.

Two candidate models were evaluated for the printer: a spectral expansion of the Yule–Nielsen–Murray–Davies equation where both the n value and reflectance factor were functions of wavelength, and a spectral expansion of the Omatsu equation where the path length of scattered light within the substrate was a function of wavelength. For both models, polynomial equations were used in preference to one-dimensional LUTs when characterizing subsystem nonlinearities. Both spectral models were combined with a dot-on-dot halftoning algorithm with 100% GCR. The model parameters were optimized based on primary and secondary color ramps, 57 samples in total. The two models had equivalent prediction accuracy. Because of its simplicity, the Yule–Nielsen–Murray–Davies based model was used to define the color gamut of the printer.

Multiple linear regression was selected to transform mathematically the scanner into an approximate imaging colorimeter when digitizing photographic reflection prints. The model consisted of a nonlinear stage that characterized the photometric nonlinearity of the scanner and a second-order 3×9 matrix that approximated the colorimetric conversion process. The model coefficients were optimized using an IT8.7/2 color target. In similar fashion to the printer models, equations were used to characterize the nonlinearities rather than one-dimensional LUTs.

The gamut mapping strategy consisted of linearly compressing the lightness range of the photographic color gamut to match the lightness range of the ink-jet color gamut. The RLAB color appearance space was used. Remaining colors outside of the compressed photographic gamut were clipped to the ink-jet gamut boundary by minimizing the interpoint distance in CIELAB (i.e., minimum ΔE^*_{ab} clipping).

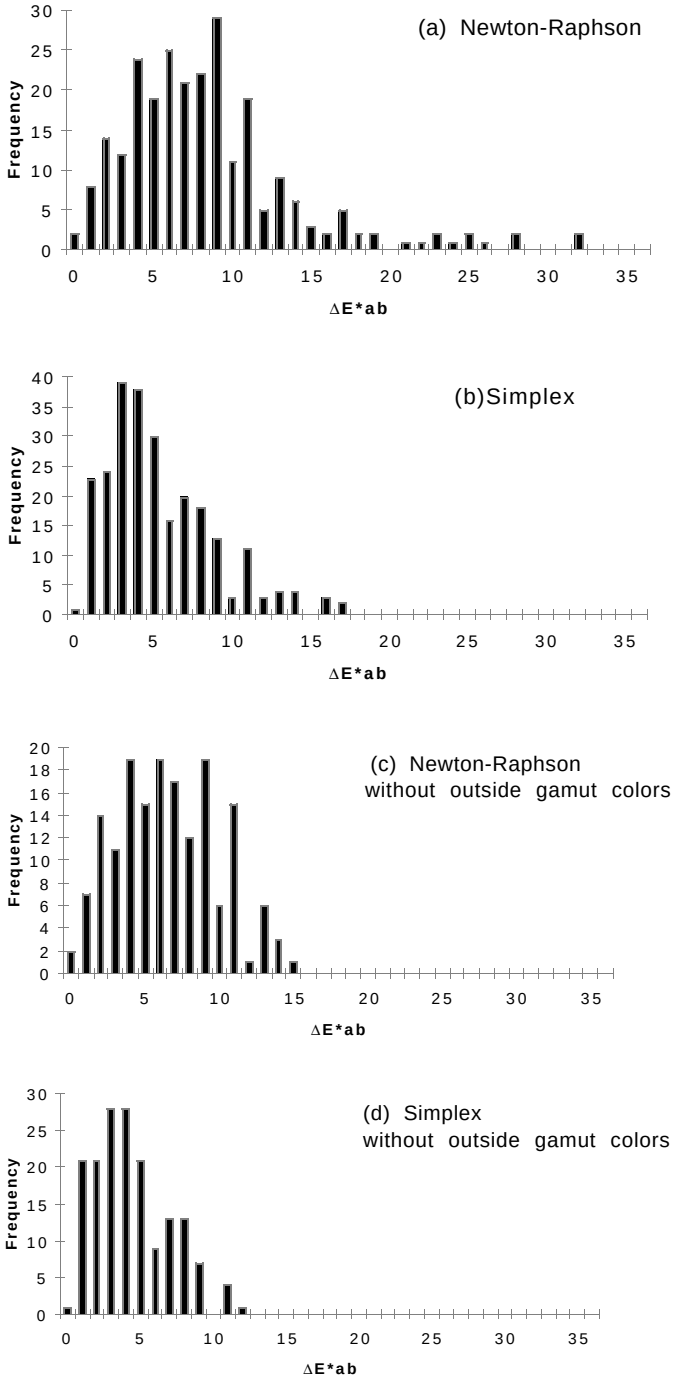

Figure 22. Color difference histograms of reproduced colors using device profiles made by the Newton–Raphson and the Simplex methods.

Perhaps the key element in building the CMM is inverting the printer forward model. That is, printer driver values (for this printer, d_r, d_g, and d_b) are required from input colorimetric data (e.g., RLAB, CIELAB, tristimulus values). Two linear optimization techniques were evaluated: the Newton–Raphson method and the Simplex algorithm. Because the Newton–Raphson method is based on calculating first derivatives, equations were preferred

in comparison to one-dimensional LUTs when describing subsystem nonlinearities of a device's color gamut. This resulted in a more accurate numerical approximation when defining the derivatives and enabled a reduction in step size to 0.1 digital counts. This was critical in order to minimize oscillations and divergences. For colors well within the two color gamuts, the Newton-Raphson method always converged quickly. When the input colorimetric coordinates corresponded to the printer's color gamut boundary or beyond, convergence problems occurred because the first derivative approached zero. A step-size function, ω, was used to reduce the step size as an aid in improving convergence problems. In some cases, this resulted in convergence, though at a significant loss of computational speed. However, there were still instances of incorrect solutions. In other words, the termination condition did not correspond to the minimum ΔE^*_{ab} clipping algorithm. The Simplex algorithm is a direct search method. As such, it did not suffer from the limitations associated with calculating derivatives. However, in the gamut mapping region, it could also terminate at the wrong values if the objective function contained the usual constraint of limiting the feasible solution (digital data constrained between 0 and 255). This was alleviated by introducing a sawtooth function that constrained data extrapolation and facilitated proper convergence.

Several conclusions can be drawn from this research. The first is that model-based printer models result in an efficient method of building CMMs once the basic modeling research in performed. Having completed this research, device profiles can be easily built by printing a test target of 57 colors and measuring the spectral reflectance factor of each sample. This is an easy manual operation and can be performed each time consumables are changed.

The second conclusion concerns the choice of iterative technique. It is clear that methods based on calculating first derivatives are problematic when incorporating gamut mapping strategies. The simplex method used in this research was an effective linear optimization method. We would expect that all derivative-based methods (whether first or second derivatives) would have convergence problems for this application, though we have not tested this conclusion. Using direct search methods, one can eliminate the need for equation-based definitions of subsystem nonlinearities. This is beneficial when simple models such as polynomials do not well fit the measured data. ▲

References

1. International Color Consortium Profile Format Specification, Version 3.2, anonymous FTP: ftp://sgigate.sgi.com/pub/icc/ICC34.pdf (1997).
2. P. C. Hung, Colorimetric calibration in electronic imaging devices using a look-up-table model and interpolations, *J. Elec. Imaging* **2**, 53 (1993).
3. D. L. Spooner, Measurement of the transfer function of hardcopy color reproduction systems: a metric for comparison, in *Proc. 1992 Vol. 2 of Technical Assoc. Graphics Arts and Inter-Society Color Council*, Rochester, New York, p. 917.
4. S. I. Nin, J. M. Kasson, and W. Plouffe, Printing CIELAB images on a CMYK printer using tri-linear interpolation, *Proc. SPIE* **1670**, 316 (1992).
5. K. Kanamori, H. Kawasaki, and H. Kotera, A novel color transformation algorithm and its applications, *Proc. SPIE* **1244**, 272 (1990).
6. H. R. Kang, Color scanner calibration of reflected samples, *Proc. SPIE* **1670**, 468 (1992).
7. H. R. Kang, Color scanner calibration, *J. Imaging Sci. Tech.* **36**, 162 (1992).
8. R. S. Berns and M. J. Shyu, Colorimetric characterization of a desktop-drum scanner via image modeling, in *Proc. IS&T and SID's 2nd Color Imaging Conf.: Color Science, System and Applications*, IS&T, Springfield, VA, 1994, p. 41.
9. R. S. Berns and M. J. Shyu, Colorimetric characterization of a desktop drum scanner using a spectral model, *J. Elec. Imaging* **4,** 360 (1995).
10. M. A. Rodriguez and T. G. Stockham, Producing colorimetric data from densitometric scans, *Proc. SPIE* **1913**, 413 (1993).
11. N. Jung and C. Tralle, An alternative method of optoelectronic color analysis for slides, *Signal Process. Image Commun.* **6**, 47 (1994).
12. J. A. S. Viggiano and C. J. Wang, A novel method for colorimetric calibration of color digitizing scanner, *TAGA Proc.* p. 143, Rochester, New York (1993).
13. R. S. Berns, Spectral modeling of a dye diffusion thermal transfer printer, *J. Elec. Imaging* **2,** 359 (1993).
14. J. A. S. Viggiano, The color of halftone tints, *TAGA Proc.* p. 661 (1985).
15. J. A. S. Viggiano, *Models for the prediction of color in graphic reproduction technology*, M.S. Thesis, Rochester Institute of Technology (1987).
16. H. R. Kang, Comparison of color mixing theories for use in electronic printing, in *IS&T/SID's Color Imaging Conf.: Transforms & Transportability of Color,* IS&T, Springfield, VA, 1993, p. 78.
17. H. R. Kang, Applications of color mixing models to electronic printing, *J. Elec. Imaging* **3**, 276 (1994).
18. R. Rolleston and R. Balasubramanian, Accuracy of various types of Neugebauer model, in *Proc. IS&T and SID's Color Imaging Conference: Transforms & Transportability of Color*, IS&T, Springfield, VA, 1993, p. 32.
19. K. J. Heuberger, Z. M. Jing and S. Persiev, Color transformations and lookup tables, in *TAGA/ISCC Proc.* **2,** 863 (1992).
20. R. S. Berns, R. J. Motta, and M. E. Gorzynski, CRT colorimetry. part I: Theory and practice, *Col. Res. Appl.* **18**, 299 (1993).
21. R. S. Berns, Methods for characterizing CRT displays, *Displays* **16**, 173 (1996).
22. P. G. Engeldrum, Four color reproduction theory for dot formed imaging systems, *J. Imaging Technol.* **12**, 126 (1986).
23. D. Q. McDowell, Summary of IT8/SC4 color activities, *Proc. SPIE* **1909**, 229 (1993).
24. American Society for Testing and Materials, *Standard test method for computing the colors of objects by using the CIE system*, ASTM Designation: E 308, Philadelphia, Pennsylvania, (most recent version).
25. A. Murray, Monochrome reproduction in photoengraving, *J. Franklin Inst.* **221,** 721 (1936).
26. J. A. C. Yule and W. J. Nielsen, The penetration of light into paper and its effect on halftone reproduction, *TAGA Proc.* p. 65, Rochester, New York (1951).
27. I. Pobboravsky and M. Pearson, Computation of dot areas required to match a colorimetrically specified color using the modified Neugebauer equations, *TAGA Proc.* p. 917, Rochester, New York (1972).
28. H. E. J. Neugebauer, Die theoretischen grundlagen des mahrfarbenbuchdrucks, *Z. Wiss. Phot.* **36**(4) 73 (1937).
29. M. Pearson, n-value for general conditions, *TAGA Proc.* p. 415, Rochester, New York (1980) .
30. L. Wilkinson, *SYSTAT: The System for Statistics*, SYSTAT, Inc., Evanston, IL 1989.
31. R. S. Berns and K. Iino, Spectral modeling of a ink-jet printer, *Elec. Imaging, SPIE/IS&T Int'l. Tech. Working Gr. Newsletter* **5**, 3 (1995).
32. T. Omatu, Y. Iketaki, S. Sakai, and M. Nishikawa, Study of color reproduction model in consideration of the effect of light scattering on a paper in color printing systems, *J. Elec. Inf. Commun. Eng.* **J69-D**, 1639 (1986) in Japanese.
33. R. S. Berns, Calorimetric characterization in of Sharp JX610 desktop scanner V2.0, *Munsell Color Science Laboratory Tech. Report,* Rochester, New York (1994).
34. P. C. Hung, Colorimetric calibration for scanners and media, *Proc. SPIE* **1448**,164 (1991).
35. J. Taft and N. Moroney, *Documentation for RITRC 3D LUT Version 1.0 for Alpha Release*, RIT Research Corporation, Rochester, NY (1994).
36. R. S. Berns, Color WYSIWYG: a combination of device colorimetric characterization and appearance modeling, *Proc. SID*, Playa del Rey, CA, 549 (1992).
37. M. D. Fairchild, Some hidden requirements for device-independent color imaging, *Proc. SID*, p. 865 Playa del Rey, CA (1994).
38. J. J. Sara, *The Automated Reproduction of Pictures with Non-reproduction Colors*, Ph.D. Thesis, Massachusetts Institute of Technology (1984).
39. J. Gordon, Richard Holub, and R. Poe, On the rendition of unprintable colors, *TAGA Proc.* p. 186 (1987).
40. M. C. Stone, W. B. Cowan and J. C. Beatty, Color gamut mapping and the printing of digital color images, *ACM Trans. Graphics* **7**, 249 (1988).
41. J. Meyer and B. Barth, Color gamut matching for hard copy, *Proc. SID*, p. 86Playa del Rey, CA (1989).
42. W. E. Wallace and M. C. Stone, Gamut mapping computer generated imagery, *Proc. SPIE* **1460**, 20 (1991).
43. T. Hoshino and R. S. Berns, Color gamut mapping techniques for color hard copy images, *Proc. SPIE* **1909,** 152 (1993).
44. M. Wolski, J. P. Allebach and C. A. Bouman, Gamut mapping squeezing the most out of your color system, in *Proc. IS&T and SID's 2nd Color Imaging Conf.: Color Science, System and Applications*, IS&T, Springfield, VA, 1994, p. 89.
45. E. D. Montag and M. D. Fairchild, Simulated color gamut mapping using simple rendered images, *Proc. SPIE* **2658,** 316 (1993).
46. M. D. Fairchild, Refinement of the RLAB color space, *Color Res. Appl.* **21**, 338 (1996).

47. M. L. James, G. M. Smith, and J. C. Wolford, *Applied Numerical Methods for Digital Computation with FORTRAN and CSMP*, 2nd Ed., Harper & Row, New York 1977.
48. N. Ohta, *Shikisai Kogaku (Color Technology)*, Tokyo Denki-daigaku Shyppan-kyoku, Tokyo, 1993, in Japanese.
49. N. Ohta, Fast computing of color matching by means of matrix representation. part I: transmission-type colorant, *Appl. Opt.* **10**, 2183 (1971).
50. N. Ohta, Fast computing of color matching by means of matrix manipulation, part II. reflection-type color print, *J. Opt. Soc. Amer.* **62**, 129 (1972).
51. H. Okumura, *Software Technology: Algorithm Thesaurus in C*, Gijyutsu Hyoron sha, Tokyo, 1991, in Japanese.
52. W. H. Press, S. A. Teukolsky, W. T. Vetterling, and B. P. Flannery, *Numerical Recipes in C*, Cambridge University Press, Cambridge, MA 1988.
53. J. Kowalik and M. R. Osborne, *Methods for Unconstrained Optimization Problems*, Elsevier, New York,1968.
54. N. Ohta, Color matching in subtractive color photography (II) metameric color matching by nonlinear optimization, *Sci. Publi. Fuji Photo Film Co., Ltd.* **20**, 107 (1973); *J. Soc. Photographic Sci. Tech. Japan* **36**, 187 (1973), in Japanese.
55. M. Stokes, M. D. Fairchild, and R. S. Berns, Colorimetrically quantified visual tolerances for pictorial images, *TAGA Proc.*, 757 (1992).
56. S. Stamm, An investigation of color tolerance, *TAGA Proc.*, Rochester, New York, 156 (1981).